Atmospheric Carbon Dioxide Concentration Across the Mid-Pleistocene Transition

Bärbel Hönisch *et al.*

Science **324**, 1551 (2009);
DOI: 10.1126/science.1171477

Science (print ISSN 0036-8075; online ISSN 1095-9203) is published weekly, except the last week in December, by the American Association for the Advancement of Science, 1200 New York Avenue NW, Washington, DC 20005.

with the (r_{12})MRCI curve of Gdanitz (*15*) indicates that this ab initio method, combined with a large basis set, recovered the true shape of the potential. The differences between Spirko's (*20*) potential energy curve and the fitted potential are too small to be seen as the scale of the plot shown in Fig. 3. To illustrate the differences, the vibrational energies and rotational constants generated from Spirko's (*20*) potential can be compared with the present results in Table 1. The close agreement shows that the reduced potential curve model is capable of achieving near spectroscopic accuracy.

The shape of the Be_2 potential energy curve is quite different from that of a standard Morse-like potential, and it is equally far away from a simple physical potential such as the Lennard-Jones model. Be_2 is unique in this respect as the related dimers of closed-shell metal atoms Mg_2 (*27*), Ca_2 (*28*), Zn_2 (*21*, *29*), and Hg_2 (*29*) exhibit typical Morse–van der Waals type potentials.

The measurements reported here resolve the question of the dissociation energy for $Be_2(X)$ and define the potential energy curve for internuclear distances less than 8.5 Å. The unusual shape of the attractive limb of the ground-state potential reflects the evolution of the configurational mixing that occurs as the atoms approach. Hence, Be_2 shows atoms passing through stages of orbital hybridization as they form an incipient chemical bond. Theoretical analyses indicate that chemical and physical interactions are finely balanced at the equilibrium distance (*14*, *17*, *30*). As a result, the Be_2 molecule has a weak bond, but a bond length that is more characteristic of a conventional covalent interaction. Our experimentally determined potential energy curve establishes a benchmark for tests of high-level theoretical methods for treatment of configurational mixing and electron correlation. Given that such interactions are also especially important in the treatment of excited electronic states and transition state regions of the potential energy surface, one can hope to assess the reliability of quantum chemical methods in situations where they are applied to regions of the potential energy surface that are not easily probed by experiment.

References and Notes

1. G. Herzberg, *Z. Phys.* **57**, 601 (1929).
2. L. Herzberg, *Z. Phys.* **84**, 571 (1933).
3. J. H. Bartlett Jr., W. H. Furry, *Phys. Rev.* **38**, 1615 (1931).
4. S. Fraga, B. J. Ransil, *J. Chem. Phys.* **35**, 669 (1961).
5. S. Fraga, B. J. Ransil, *J. Chem. Phys.* **36**, 1127 (1962).
6. C. F. Bender, E. R. Davidson, *J. Chem. Phys.* **47**, 4972 (1967).
7. B. H. Lengsfield III, A. D. McLean, M. Yoshimine, B. Liu, *J. Chem. Phys.* **79**, 1891 (1983).
8. R. J. Harrison, N. C. Handy, *Chem. Phys. Lett.* **98**, 97 (1983).
9. J. M. Brom Jr., W. D. Hewett Jr., W. Weltner Jr., *J. Chem. Phys.* **62**, 3122 (1975).
10. V. E. Bondybey, J. H. English, *J. Chem. Phys.* **80**, 568 (1984).
11. V. E. Bondybey, *Chem. Phys. Lett.* **109**, 436 (1984).
12. V. E. Bondybey, *Science* **227**, 125 (1985).
13. I. Røeggen, J. Almlöf, *Int. J. Quantum Chem.* **60**, 453 (1996).
14. S. Evangelisti, G. L. Bendazzoli, L. Gagliardi, *Chem. Phys.* **185**, 47 (1994).
15. R. J. Gdanitz, *Chem. Phys. Lett.* **312**, 578 (1999).
16. J. M. L. Martin, *Chem. Phys. Lett.* **303**, 399 (1999).
17. A. Krapp, F. M. Bickelhaupt, G. Frenking, *Chem. Eur. J.* **12**, 9196 (2006).
18. G. A. Petersson, W. A. Shirley, *Chem. Phys. Lett.* **160**, 494 (1989).
19. S. Evangelisti, G. L. Bendazzoli, R. Ansaloni, F. Duri, E. Rossi, *Chem. Phys. Lett.* **252**, 437 (1996).
20. V. Spirko, *J. Mol. Spectrosc.* **235**, 268 (2006).
21. K. Patkowski, R. Podeszwa, K. Szalewicz, *J. Phys. Chem. A* **111**, 12822 (2007).
22. J. M. Merritt, A. L. Kaledin, V. E. Bondybey, M. C. Heaven, *Phys. Chem. Chem. Phys.* **10**, 4006 (2008).
23. Materials and methods are available as supporting material on *Science* Online.
24. F. J. Northrup, T. J. Sears, *Annu. Rev. Phys. Chem.* **43**, 127 (1992).
25. R. J. LeRoy, J. Y. Seto, Y. Huang, *DPotFit; A Computer Program for Fitting Diatomic Molecular Spectral Data to Potential Energy Functions* (University of Waterloo Chemical Physics Research Report CP-662R, Waterloo, Ontario, Canada, 2006).
26. R. J. Le Roy *et al.*, *J. Chem. Phys.* **123**, 204304 (2005).
27. E. Czuchaj, M. Krosnicki, H. Stoll, *Theor. Chem. Acc.* **107**, 27 (2001).
28. E. Czuchaj, M. Krosnicki, H. Stoll, *Theor. Chem. Acc.* **110**, 28 (2003).
29. L. Bucinsky, S. Biskupic, M. Ilcin, V. Lukes, V. Laurinc, *J. Comput. Chem.* **30**, 65 (2008).
30. I. Røeggen, K. Morokuma, K. Yamashita, *Chem. Phys. Lett.* **140**, 349 (1987).

31. We are grateful for the financial support of this work provided by NSF (grant CHE-0518094). V.E.B. thanks Die Deutsche Forschungsgemeinschaft for partial support of his visit to Emory University.

Supporting Online Material

www.sciencemag.org/cgi/content/full/1174326/DC1
Materials and Methods
Fig. S1
References

31 March 2009; accepted 6 May 2009
Published online 21 May 2009;
10.1126/science.1174326
Include this information when citing this paper.

Atmospheric Carbon Dioxide Concentration Across the Mid-Pleistocene Transition

Bärbel Hönisch,[1] N. Gary Hemming,[1,2] David Archer,[3] Mark Siddall,[4] Jerry F. McManus[1]

The dominant period of Pleistocene glacial cycles changed during the mid-Pleistocene from 40,000 years to 100,000 years, for as yet unknown reasons. Here we present a 2.1-million-year record of sea surface partial pressure of CO_2 (Pco_2), based on boron isotopes in planktic foraminifer shells, which suggests that the atmospheric partial pressure of CO_2 (pco_2) was relatively stable before the mid-Pleistocene climate transition. Glacial Pco_2 was ~31 microatmospheres higher before the transition (more than 1 million years ago), but interglacial Pco_2 was similar to that of late Pleistocene interglacial cycles (<450,000 years ago). These estimates are consistent with a close linkage between atmospheric CO_2 concentration and global climate, but the lack of a gradual decrease in interglacial Pco_2 does not support the suggestion that a long-term drawdown of atmospheric CO_2 was the main cause of the climate transition.

The mid-Pleistocene transition (MPT) is the period around 1250 to 700 thousand years ago (ka), when global climate variability changed from the dominant 40-thousand-year (ky) orbital period of the Pliocene/early Pleistocene to the 100-ky ice-age cycles of the past 700 ky (*1*–*3*). Orbital variation does exert some forcing on the 100-ky time scale, but it is relatively weak and seems a feeble explanation for the 100-ky ice ages. The change in periodicity was accompanied by a gradual increase in value and amplitude of the oxygen isotopic composition of benthic foraminifer shells, suggesting that total ice volume increased and/or deep-water temperatures probably decreased over the MPT (*3*, *4*). It has been suggested the MPT was caused by global cooling, possibly due to a long-term decrease in atmospheric CO_2 concentrations (*5*), but the evidence is inconclusive. Sea surface temperature (SST) estimates from eastern basin upwelling areas (*6*–*9*) are consistent with substantial cooling, but estimates from the western Pacific warm pool (WPWP) indicate relatively stable temperatures across the transition (*10*, *11*). Because the WPWP is an area particularly sensitive to changes in radiative forcing, that temperature stability has been used to argue that a secular decrease in atmospheric partial pressure of CO_2 (pco_2) did not occur (*10*). In contrast, another study observed higher glacial SSTs before the MPT and ascribed these to changes in greenhouse forcing (*11*). Thus, there currently is no direct evidence substantiating any long-tem trend in pco_2.

The most accurate archive for atmospheric pco_2 comes from ancient air trapped in polar ice. Ice core records reveal that pco_2 varied between

[1]Department of Earth and Environmental Sciences, Lamont-Doherty Earth Observatory of Columbia University, NY 10964–8000, USA. [2]School of Earth and Environmental Sciences, Queens College, New York, NY, 11367–1597, USA. [3]Department of Geophysical Sciences, University of Chicago, Chicago, IL 60637, USA. [4]Department of Earth Sciences, University of Bristol, Bristol, UK.

180 and 300 parts per million by volume (ppmv) during the last four glacial cycles (*12*) and between 172 and 260 ppmv for the period from 800 to 450 ka (*13*, *14*). Contrary to the suggestion that pCO_2 decreased toward the late Pleistocene, the earlier pCO_2 amplitude and average were lower than in the more recent past. However, existing ice core records are limited to the past 800 ky, and no ice core data are available for the full duration of the MPT.

Because CO_2 is well mixed in the atmosphere over the time scale of a few years, and because CO_2 is exchanged rapidly between the surface ocean and atmosphere, marine proxy records of past sea surface carbonate chemistry can place constraints on past atmospheric pCO_2. The boron isotopic composition of planktic foraminifer shells is a proxy for past seawater pH. This proxy is based on the equilibrium reaction between the two dominant species of dissolved boron in seawater and the isotope fractionation between the two species [supporting online material (SOM)]. Atmospheric pCO_2 can be estimated from the boron isotopic composition of those shells if (i) aqueous partial pressure of CO_2 (PCO_2) at the core site is in equilibrium with atmospheric pCO_2, and (ii) another carbon parameter of the water in which the foraminifers grew is known. Using reasonable assumptions about seawater alkalinity, quantitative replication of select intervals of the Vostok pCO_2 record from boron isotopes in the planktic foraminifer *Globigerinoides sacculifer* (*15*) has demonstrated the validity of this method.

Here, we extend the existing 400-ky boron isotope record from Ocean Drilling Program (ODP) site 668B beyond the MPT to 2.1 million years ago. ODP site 668B is located on the Sierra Leone Rise in the eastern equatorial Atlantic (4°46′N, 20°55′W) at a water depth of 2693 m. Nearby oceanographic data (from World Ocean Circulation Experiment cruise A15, station 34) indicate that in the modern ocean, aqueous PCO_2 and atmospheric pCO_2 are in equilibrium. Reconstruction of the local marine carbonate chemistry thus allows us to estimate PCO_2 and infer pCO_2.

From this sediment core, we constructed a high-resolution oxygen isotope ($\delta^{18}O$) record from shells of the surface-dwelling *G. ruber*. The record allows us to establish an age model, which is simultaneously tied (*16*) to the stack of 57 globally distributed benthic $\delta^{18}O$ records [the LR04 stack (*4*)] and the planktic $\delta^{18}O$ record of ODP site 677 (*17*). Large *G. sacculifer* shells were selected from extreme glacial and interglacial samples and transitional periods for boron isotope analysis (fig. S1 and SOM). Boron isotopes were measured by negative thermal ionization mass spectrometry and complemented by Mg/Ca analyses on small shells of *G. ruber* for temperature reconstruction (see SOM for further details). Boron isotope data were then converted into pH estimates, using the empirical calibration for *G. sacculifer* (*18*) and following the procedure outlined in (*15*). Mg/Ca-based SSTs were estimated according to the method of (*19*). The salinity effect on Mg/Ca temperature estimates discovered by (*20*) has been considered but found to be of negligible importance for PCO_2 estimates (SOM).

In order to translate the pH estimates into PCO_2, a second parameter of the carbonate system is required, such as $[CO_3^{=}]$ or alkalinity. An evaluation of methods to estimate this second param-

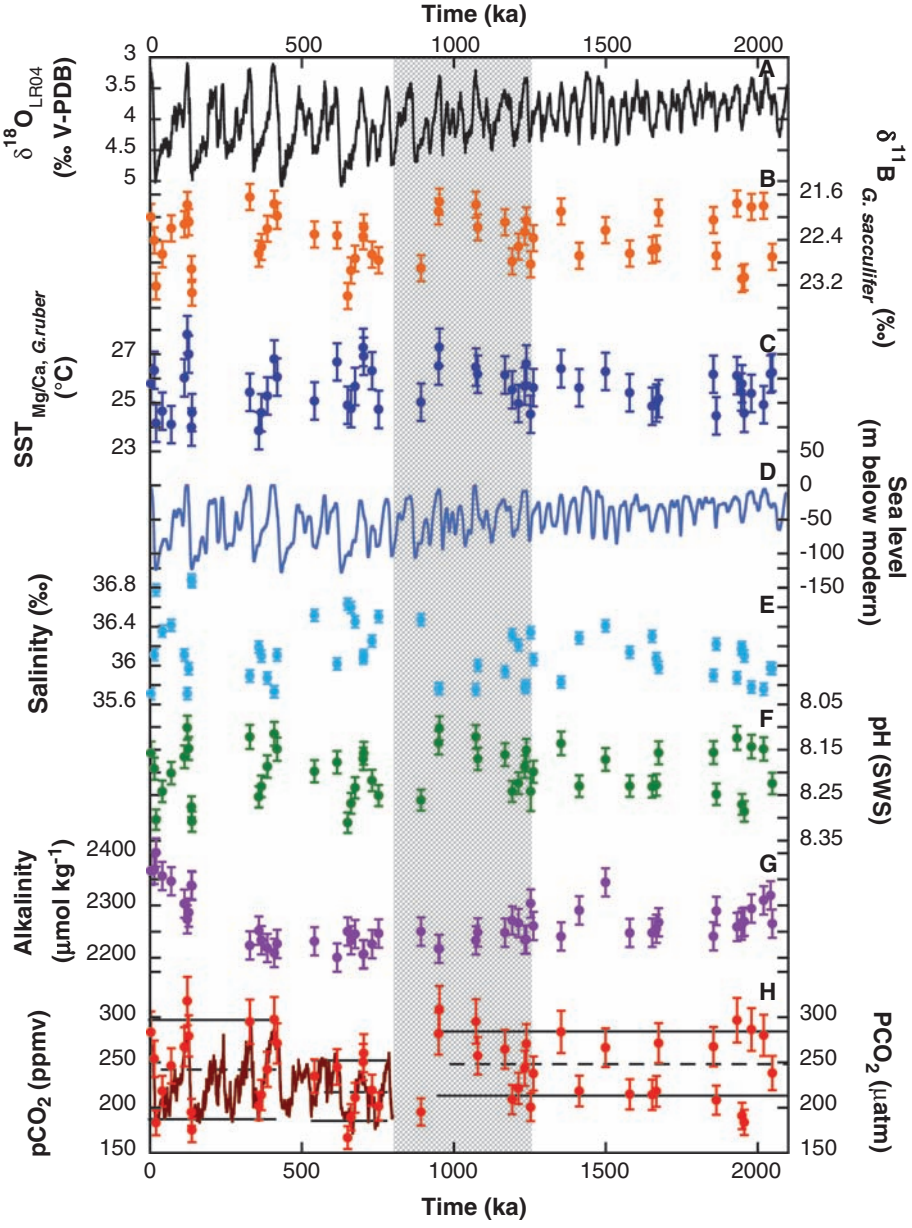

Fig. 1. 2.1-million-year estimation of atmospheric pCO_2 from marine proxies recorded at ODP site 668B in the eastern equatorial Atlantic. (**A**) The LR04 benthic oxygen isotope stack (*4*) reflects the change from the dominant 40-ky periodicity of glacial cycles before 1200 ka to the 100-ky ice-age cycles of the past 700 ky. The MPT is indicated by the horizontal gray bar and describes the transition period. (**B**) Planktic $\delta^{11}B$ data reflect extreme glacial and interglacial times and few transitional periods, selected from the $\delta^{18}O$ record, and are complemented by (**C**) Mg/Ca SST estimates and (**E**) local salinity estimates computed from (**D**) modeled global sea level (*21*). (**F**) Surface seawater pH on the seawater scale (SWS) was calculated as a function of $\delta^{11}B$, SST, and salinity. (**G**) Alkalinity estimates are based on a modeled global ocean estimate (*3*), adjusted to modern local alkalinity at the core site and varying sea level. (**H**) Surface ocean aqueous PCO_2 was then calculated as a function of pH, alkalinity, SST, and salinity. Comparison with the ice core record of atmospheric pCO_2 [dark red line in (H)] reveals a remarkable match for the period from 800 ka to the present. Average glacial and interglacial PCO_2 is indicated by solid horizontal black lines for different intervals in (H). Dashed lines indicate G/I averages. Error bars indicate the propagated error of the individual pH, SST, salinity, and alkalinity uncertainties on the PCO_2 estimate (see SOM for details).

eter is given in the SOM. We followed a similar procedure to that outlined in (*15*), bracketing the potential variations in whole-ocean inventory of alkalinity between two possibilities: (i) Alkalinity remained constant in the past (constant alkalinity scenario); and (ii) alkalinity varied as a function of past terrestrial weathering, ocean $CaCO_3$ production, and sediment dissolution rates [varying alkalinity scenario, after (*3*)]. The degree to which local salinity and alkalinity were increased during glacial periods, when sea level was lower, was approximated with the global sea-level estimate determined by (*21*) relative to average ocean depth (see the SOM for further details and additional validation of this approach).

The pH, temperature, and Pco_2 estimates are shown in Fig. 1. The pre-MPT ocean chemistry revealed from $\delta^{11}B$ is characterized by less basic glacials (pH 8.24 ± 0.03, 1 SD) relative to the post-MPT (pH 8.29 ± 0.02), whereas interglacial pH is comparable between the two intervals (pH 8.14 ± 0.02 and 8.14 ± 0.03, respectively). Several uncertainties were considered for the Pco_2 calculation (SOM) but were found to be of minor importance. The only significant Pco_2 difference stems from the choice of alkalinity, where a total difference in alkalinity of up to 221 μmol kg^{-1} between scenarios results in a maximum Pco_2 difference of 27 microatmospheres (μatm) and an average difference of 17.7 μatm (fig. S1 and SOM). The Pco_2 estimates presented here are based on the varying alkalinity scenario [after (*3*)], in which weathering of the Canadian Shield modulates 4% of global weathering rates. Although all Pco_2 estimates are very similar, this one yields the best match with the measured atmospheric pco_2 over the past 800 ky (fig. S1 and SOM). According to this scenario, our proxy estimates translate into pre-MPT interglacial Pco_2 similar to that of the most recent interglacials (283 μatm) but relatively higher pre-MPT glacial Pco_2 (213 μatm). In comparison, the constant alkalinity scenario yields Pco_2 ~ 10 to 20 μatm higher for the entire record (fig. S1 and SOM). The large uncertainty in alkalinity thus results in only a small difference in the Pco_2 estimate and indicates that seawater pH is a a sensitive parameter for calculating Pco_2. Because changes in ocean alkalinity were probably accompanied by similar changes in total dissolved inorganic carbon, they appear to exert only a small impact.

Considering only extreme glacial/interglacial (G/I) samples, as determined by the oxygen isotope stratigraphy, the values and amplitudes of our reconstructed Pco_2 cycles show good agreement with ice core measurements (Table 1). The ice core pco_2 data for the intervals 0 to 418 ka (180 to 300 ppmv range, 239 ppmv average) and 540 to 800 ka (172 to 260 ppmv range, 221 ppmv average) (*12*–*14*) are remarkably consistent with our marine proxy estimates for those intervals (184 to 297 μatm range, 241 μatm average; and 181 to 252 atm range, 217 μatm average, respectively). In addition, the exceptionally low pco_2 (172 ppmv) measured in ice cores during marine isotope stage (MIS) 16 is reflected in a similarly low boron isotope estimate of 167 ± 13 μatm.

Our reconstructed pH and Pco_2 changes also agree well with the climate signal recorded in the LR04 stack (*4*): Extreme interglacial benthic $\delta^{18}O$ was relatively constant over the course of our 2.1-million-year record [3.2 to 3.5 per mil (‰)], but extreme glacial benthic $\delta^{18}O$ increased from 4.3‰ at 2.1 Ma to 5.1‰ for the post-MPT glacials (Fig. 1). The relatively less extreme glacials of the pre-MPT are thus reflected in a smaller land ice extent and/or warmer deep-sea temperatures and correlate well with higher glacial pco_2. Our data are also consistent with SST reconstructions from the WPWP indicating warmer glacial SSTs pre-MPT as compared to post-MPT, but similar interglacial SSTs (*11*). Strong correlations also exist between sub-Antarctic alkenone SST and ice core change in temperature and between the abundance of alkenones in ODP site 1090 and pco_2 measured in ice cores (*22*). The record covers only 1.1 million years but agrees well throughout with our boron isotope reconstruction. In particular, the alkenone record shows exceptionally high SST and exceptionally low alkenone abundance for MIS 25 (950 ka), suggesting high pco_2 of ≥300 ppm. This observation agrees well with the warmest interglacial SSTs observed in the WPWP for MIS 25 (*11*) and is consistent with our boron isotope estimate, which indicates higher than average Pco_2 (308 μatm) for MIS 25. Comparison with independent climate records of polar ice extent and deep ocean temperature (*4*), sub-Antarctic SST (*22*), and WPWP SSTs (*11*) thus corroborates the validity of our estimates and supports the notion that interglacial atmospheric pco_2 before the MPT was similar to that in the preindustrial period, but that pre-MPT glacial pco_2 was ~31 μatm higher than during post-MPT glacials.

In order to estimate climate sensitivity from the observed CO_2 changes, we focus on the pre-MPT glacials, because pre- and post-MPT interglacial Pco_2 are statistically indistinguishable (Table 1). We use a logarithmic climate sensitivity equation (*23*) with an average equilibrium temperature change of 5 K for doubling CO_2. This temperature change is at the high end of CO_2 sensitivity estimates on short time scales but is more appropriate for the longer time scales considered here, which include slow feedbacks such as ice-sheet albedo effects (*24*). Based on this sensitivity, the global average surface air temperature during pre-MPT glacials was 1.06 K warmer than during post-MPT glacials. In comparison, the mean global temperature change from the Last Glacial Maximum to the preindustrial period is 3.3 to 5.1 K [as estimated by the Paleoclimate Model Intercomparison Project (*25*)]. Consequently, the average pre-MPT G/I global temperature change was ~30% smaller than during the past 400 ky. However, the smaller temperature range does not imply a gradual decline in greenhouse forcing over the MPT. Although the average G/I pco_2 was ~7 μatm higher before the transition (Table 1), this difference is entirely a result of higher glacial pco_2. The higher glacial pco_2 is consistent with the warmer glacial SSTs, ice extent, and/or deep-sea temperatures, but interglacial pco_2 was similar before and after the transition. We therefore conclude that CO_2 was unlikely to have been the main driver of the MPT. We also conclude that present-day atmospheric pco_2 is the highest it has been for the past 2.1 million years, requiring a search for an analog for present-day conditions, possibly during the time before the acceleration of Northern Hemisphere glaciation before 2.7 million years ago.

Table 1. Comparison of glacial and interglacial pco_2 extremes as measured from ice cores (*12*–*14*) and estimated from boron isotopes in planktic foraminifers (see fig. S1 for the selection and number of data included in each average). Cumulative uncertainties have been calculated for the G/I boron isotope Pco_2 estimates, assuming that the propagated errors of individual data are normally distributed.

Interval (ka)	Ice core pco_2 (ppmv)			Boron isotope Pco_2 (μatm)		
	Minimum	Maximum	Average	Minimum	Maximum	G/I average
0–418	180	300	239	184^{+17}_{-14}	297^{+29}_{-21}	241
450–800	172	260	221	181^{+15}_{-20}	252^{+17}_{-14}	217
892–2048	–	–	–	213^{+30}_{-28}	283^{+30}_{-37}	248

References and Notes

1. J. Hays, J. Imbrie, N. Shackleton, *Science* **194**, 1121 (1976).
2. N. G. Pisias, T. C. Moore Jr., *Earth Planet. Sci. Lett.* **52**, 450 (1981).
3. P. U. Clark *et al.*, *Quat. Sci. Rev.* **25**, 3150 (2006).
4. L. E. Lisiecki, M. E. Raymo, *Paleoceanography* **20**, 10.1029/2004PA001071 (2005).
5. M. E. Raymo, W. F. Ruddiman, P. N. Froelich, *Geology* **16**, 649 (1988).
6. J. R. Marlow, C. B. Lange, G. Wefer, A. Rosell-Mele, *Science* **290**, 2288 (2000).
7. M. W. Wara, A. C. Ravelo, M. L. Delaney, *Science* **309**, 758 (2005).
8. E. L. McClymont, A. Rosell-Melé, *Geology* **33**, 389 (2005).
9. K. T. Lawrence, Z. Liu, T. D. Herbert, *Science* **312**, 79 (2006).
10. T. de Garidel-Thoron, Y. Rosenthal, F. Bassinot, L. Beaufort, *Nature* **433**, 294 (2005).
11. M. Medina-Elizalde, D. W. Lea, *Science* **310**, 1009 (2005).
12. J. R. Petit *et al.*, *Nature* **399**, 429 (1999).
13. U. Siegenthaler *et al.*, *Science* **310**, 1313 (2005).
14. D. Lüthi *et al.*, *Nature* **453**, 379 (2008).
15. B. Hönisch, N. G. Hemming, *Earth Planet. Sci. Lett.* **236**, 305 (2005).
16. D. Paillard, L. Labeyrie, P. Yiou, *Eos* **77**, 379 (1996).
17. N. J. Shackleton, A. Berger, W. A. Peltier, *Trans. R. Soc. Edinb. Earth Sci.* **81**, 251 (1990).
18. A. Sanyal, J. Bijma, H. J. Spero, D. W. Lea, *Paleoceanography* **16**, 515 (2001).
19. P. S. Dekens, D. W. Lea, D. K. Pak, H. J. Spero, *Geochem. Geophys. Geosyst.* **3**, 10.1029/2001GC000200 (2002).
20. B. Kisakürek, A. Eisenhauer, F. Böhm, D. Garbe-Schönberg, J. Erez, *Earth Planet. Sci. Lett.* **273**, 260 (2008).

21. R. Bintanja, R. S. W. van de Wal, *Nature* **454**, 869 (2008).
22. A. Martínez-Garcia *et al.*, *Paleoceanography* **24**, 10.1029/2008PA001657 (2009).
23. D. Archer, *Global Warming—Understanding the Forecast* (Blackwell Publishing, Malden, MA, 2006).
24. J. Hansen *et al.*, *Open Atm. Sci. J.* **2**, 217 (2008).
25. E. Jansen *et al.*, in *Climate Change 2007: The Physical Science Basis. Contribution of Working Group I to the Fourth Assessment Report of the Intergovernmental Panel on Climate Change,* S. Solomon *et al.*, Eds. (Cambridge Univ. Press, Cambridge, 2007).

26. We thank ODP for sediment samples and NSF (grant OCE 06-23621) for financial support. The idea for this study was seeded through conversations with S. Hemming. L. Leon is gratefully acknowledged for laboratory assistance, P. deMenocal for Mg/Ca analyses at the Lamont-Doherty Earth Observatory (LDEO), and M. Segl for isotope analyses at Bremen University. We also thank C. Pelejero and two anonymous reviewers for valuable comments. Discussions with P. Köhler and R. Bintanja improved the manuscript. The oxygen isotope data are available in the National Oceanic and Atmospheric Administration Paleoclimatology database (www.ngdc.noaa.gov/paleo/data.html). This is LDEO contribution number 7261.

Supporting Online Material
www.sciencemag.org/cgi/content/full/324/5934/1551/DC1
Materials and Methods
Figs. S1 and S2
Table S1
References

27 January 2009; accepted 6 May 2009
10.1126/science.1171477

Fossil Plant Relative Abundances Indicate Sudden Loss of Late Triassic Biodiversity in East Greenland

Jennifer C. McElwain,[1]* Peter J. Wagner,[2] Stephen P. Hesselbo[3]

The pace of Late Triassic (LT) biodiversity loss is uncertain, yet it could help to decipher causal mechanisms of mass extinction. We investigated relative abundance distributions (RADs) of six LT plant assemblages from the Kap Stewart Group, East Greenland, to determine the pace of collapse of LT primary productivity. RADs displayed not simply decreases in the number of taxa, but decreases in the number of common taxa. Likelihood tests rejected a hypothesis of continuously declining diversity. Instead, the RAD shift occurred over the upper two-to-four fossil plant assemblages and most likely over the last three (final 13 meters), coinciding with increased atmospheric carbon dioxide concentration and global warming. Thus, although the LT event did not induce mass extinction of plant families, it accompanied major and abrupt change in their ecology and diversity.

Ecological theory shows that relative abundance distributions (RADs) provide important information on the ecological assembly rules for communities in both the present (*1*, *2*) and past (*3*). The general ecological rules that underpin community assembly are also independent of species composition, thus providing a metric of past diversity that is applicable to communities of disparate composition, phylogenetic history, and age (*1*, *2*). Differences among RADs reflect differences in dominance and rarity as well as richness. RADs describe dominance and rarity more exactly than does evenness (i.e., uniformity of abundances) alone (*4*). Hypotheses of ecological deterioration make predictions about changes in RADs over time without necessarily predicting extinction (*5*, *6*). Therefore, if prolonged ecological deterioration precedes a mass extinction, then RADs could reveal ecological deterioration better than richness or evenness alone.

We use RADs to examine the pace of diversity loss leading to the Triassic-Jurassic boundary (TJB). The TJB extinction is one of the five greatest in Earth history (*7*), but the pace of biodiversity loss remains uncertain (*8*–*12*). This hampers our ability to distinguish between competing hypotheses on the causal mechanisms of the TJB mass extinction. Gradual extinction patterns have been reported. RADs offer an opportunity to reexamine the pace of LT biodiversity change in greater detail than provided by either changes in richness or evenness.

We assessed trends in RADs over six taphonomically similar Rhaetian aged fossil plant beds from Astartekløft, East Greenland (*10*). First, we determined the most likely RAD model for each bed based on the expected number of taxa with x specimens given the observed sample size (*3*). We considered four RAD models: geometric and the zero-sum multinomial, which are governed largely by ecological succession (*1*, *2*); and lognormal and Zipf, which are governed by increasing ecospace due to facilitation or niche construction (*1*). Because the different RADs do not represent special cases of each other, we use Akaike's modified information criterion to choose the best model (*3*, *13*).

Second, we assessed a series of increasingly complicated temporal models of LT plant diversity change. We did this by assessing the likelihood of a range of models, and thus the joint likelihood that 2+ assemblages shared the same RAD. Because not all beds fit the same RAD model, we labeled each model with a more general aspect of diversity: the hypothesized number of genera (S) with frequency greater than 10^{-6} ($S_{f>10^{-6}}$). In order of increasing complexity, we considered (i) uniform diversity over the whole Rhaetian-aged portion of the Astartekløft section ($\Delta S_{f>10^{-6}} = 0$); (ii) linear diversity decrease over the same interval ($\Delta S_{f>10^{-6}} < 0$); (iii) static diversity followed by linear decrease in the later Rhaetian portion of the section; (iv) static diversity followed by curvilinear decrease in the later Rhaetian portion of the section.

The simpler temporal models are special cases of the more complicated temporal models. Thus, we can use log-likelihood ratios to test whether a more complicated temporal model is significantly better than a simpler one (*14*). We tested hypothesized RAD shifts by how well those hypotheses predict observed abundances given the best general RAD model and the hypothesized shift in $S_{f>10^{-6}}$, not by how well they predict the best exact model. Second, we reach identical conclusions using $S_{f>10^{-5}}$ or $S_{f>10^{-4}}$.

Table 1. Modified Akaike's information criteria (AICc) for best examples of each general RAD model. AICc = $-2 \times \ln L[H|data] \times n/(n - k - 1)$, where H is the best hypothesis from each model, n is the number of specimens, and k is the number of parameters ($k = 1$ for geometric; otherwise $k = 2$). The lowest AICc value (bold) gives the best fit (*13*).

			RAD model AICc			
Bed	Taxa	n	Geometric	Zero sum	Lognormal	Zipf
1	13	224	**91.6**	96.9	97.2	123.3
1.5	9	62	**50.8**	54.4	52.6	52.4
2	12	258	**96.8**	99.0	98.9	107.6
3	9	525	68.0	124.3	**62.3**	62.6
4	11	876	**96.1**	97.5	124.3	162.5
5A	7	275	**52.4**	60.9	63.4	76.1

[1]UCD School of Biology and Environmental Science, University College Dublin, National University of Ireland, Belfield, Dublin 4, Ireland. [2]Department of Paleobiology, National Museum of Natural History, Smithsonian Institution, Washington, DC 20560, USA. [3]Department of Earth Sciences, University of Oxford, Oxford OX1 3PR, UK.

*To whom correspondence should be addressed. E-mail: jennifer.mcelwain@ucd.ie